https://dx.doi.org/10.1016/j.scitotenv.2019.04.075

Photochemical evolution of continental air masses and their influence on ozone formation over the South China Sea

Yu Wang[1], Hai Guo*, [1], Xiaopu Lyu[1], Luyao Zhang[1], Yangzong Zeren[1], Shichun Zou**, [2], Zhenhao Ling[3]

[1] Air Quality Studies, Department of Civil and Environmental Engineering, The Hong Kong Polytechnic University, Hong Kong, China

[2] School of Marine Sciences, Sun Yat-sen University, China

[3] School of Atmospheric Sciences, Sun Yat-sen University, China

* Corresponding author: ceguohai@polyu.edu.hk

** Second corresponding author: ceszsc@mail.sysu.edu.cn

Abstract

To investigate photochemical ozone (O_3) pollution over the South China Sea (SCS), an intensive sampling campaign was conducted from August to November simultaneously at a continental site (Tung Chung, TC) and a marine site (Wan Shan Island, WSI). It was found that when continental air masses intruded the SCS, O_3 episodes often occurred subsequently. To discover the causes, a photochemical trajectory model (PTM) coupled with the near-explicit Master Chemical Mechanism (MCM) was adopted, and the photochemical processes of air masses during the transport from TC to WSI were investigated. The simulated O_3 and its precursors (*i.e.* NO_x and VOCs) showed a reasonably good agreement with the observations at both TC and WSI, indicating that the PTM was capable of simulating O_3 formation for air masses traveling from TC to WSI. The modeling results revealed that during the transport of air masses from TC to WSI, both VOC and NO_x decreased in the morning while O_3 increased significantly, mainly due to rapid chemical reactions with elevated radicals over the SCS. The elevated radicals over the SCS were attributable to the fact that higher NO_x at TC consumed more radicals, whereas the concentration of radicals increased

from TC to WSI because of NO_x dilution and destruction. Subsequently, the photochemical cycling of radicals accelerated, leading to high O_3 mixing ratios over the SCS.

Furthermore, based on the source profiles of the emission inventory used, the contributions of six sources, *i.e.* gasoline vehicle exhaust, diesel vehicle exhaust, gasoline evaporation and LPG usage, solvent usage, biomass and coal burning, and biogenic emissions, to maritime O_3 formation were evaluated. The results suggested that gasoline vehicles exhaust and solvent usage largely contributed the O_3 formation over the SCS (about 5.2 and 3.8 ppbv, respectively). This is the first time that the contribution of continental VOC sources to the maritime O_3 formation was quantified.

Keywords: Ozone; Continental air masses; VOC sources; Photochemical Trajectory Model; South China Sea

1 Introduction

Surface ozone (O_3) is a secondary pollutant which has large detrimental effect on human health, visibility and climate change (NRC, 1991; Seinfeld and Pandis, 2016). Ozone pollution involves many aspects, such as emissions of precursors (*i.e.* volatile organic compounds (VOCs) and nitrogen oxides (NO_x = NO + NO_2)), photochemical formation and dynamic transport on different scales, making it a complex phenomenon (Jacob, 1999; Guo *et al.*, 2017). O_3 precursors emitted in urban areas can not only cause photochemical smog in the source region, but also travel to broad remote areas, resulting in increased O_3 in these downwind receptor regions (Finlayson-Pitts and Pitts, 1993; Solberg *et al.*, 2004). In addition, the emission sources of these primary precursors are variable, making O_3 pollution more complicated (Guo *et al.*, 2017). Thus, understanding the emission sources of precursors and their impact on O_3 formation, and subsequently formulating and implementing control measures are critical to mitigate O_3 pollution.

With high emissions of VOCs and NO_x, the fast developing Pearl River Delta (PRD) region, including Hong Kong and Macau, has suffered from high O_3 pollution during the last three decades (Wang *et al.*, 1998; Guo *et al.*, 2009; Wang *et al.*, 2009; Xue *et al.*, 2014; Li *et al.*, 2014; Wang *et al.*, 2017a, b). Numerous studies have focused on the VOC source apportionments in this region, which well elaborated VOC sources and their impact on O_3 formation (Zhang *et al.*, 2007; Guo *et al.*, 2017). For example, Guo *et al.* (2004) first probed the sources of VOCs in urban Hong Kong and found that vehicle exhaust was the dominant sources of VOCs, followed by solvent usage, natural gas/liquefied petroleum gas (LPG) leakage and industrial emissions. Based on VOCs observations at seven sites in the PRD, Liu *et al.* (2008) identified 12 sources and confirmed that vehicular exhaust made the highest contribution (~50% of ambient VOCs) at the urban sites while solvent usage was remarkable (~30%) at an industrial and a non-urban sites. A long-term study during 2005–2014 conducted at a suburban site in Hong Kong concluded that the two major sources of VOCs, *i.e.* solvent-related (~55%) and traffic-related sources (~45%), had no significant changes over the period (Ou *et al.*, 2015). Moreover, Ling *et al.* (2011) assessed the relative contribution of VOC sources to O_3 formation at a suburban site of PRD and demonstrated that solvent usage, diesel vehicular emissions and biomass/biofuel burning were the key contributors to the O_3 formation. Based on the measurements at an urban site in autumn 2010, Ling and Guo (2014) found that paint and sealant solvents, diesel exhaust and LPG usage contributed most to O_3 formation in urban Hong Kong.

Compared to urban locations, O_3 levels are often greater in remote areas such as mountainous (Guo *et al.*, 2013; Lam *et al.*, 2013) and oceanic areas (Wang *et al.*, 2018a, b). Guo *et al.* (2013) revealed the association of high O_3 concentrations observed at a mountainous site of Hong Kong with the urban emissions from the foot of the mountain where urban centre is located. Lam *et al.* (2013) further applied a moving box model to evaluate the impact of

VOCs emitted from urban sources (*i.e.* mountain foot) on the O_3 formation at the receptor site (*i.e.* mountain summit) under the influence of mountain-valley breezes. They found that vehicular emissions from the foot of the mountain were the dominant VOC sources contributing to O_3 formation at the mountain summit. Different from the causes of O_3 formation in mountainous areas, the interaction between continental and maritime air such as sea-land breezes sometimes forms weak circulation cells in which pollutants become entrained, enhancing the O_3 formation in coastal areas of the PRD region (Wang *et al.*, 2018a). Furthermore, Wang *et al.* (2018b) confirmed that O_3 precursors effused to the maritime atmosphere elevated OH radicals, and accelerated the photochemical reaction cycling processes, resulting in enhanced photochemical O_3 production. In this study, although the high O_3 pollution over the SCS is recognized, how the emissions of O_3 precursors in the continental PRD affect the O_3 formation over the maritime atmosphere remains unclear.

To tackle the air pollution problems in the study region, a Photochemical Trajectory Model coupled with near-explicit Master Chemical Mechanism (PTM-MCM) was developed to simulate O_3 mixing ratios and the processes of O_3 photochemistry during the transport of continental O_3 precursors from coastal PRD region to the SCS. Furthermore, the contributions of individual continental VOC sources to O_3 formation during their transport to the SCS were evaluated, and some control policy suggestions were provided accordingly.

2 Methodology

2.1 Sampling site

In order to understand the chemical evolution of air masses during the transport from continental source region to maritime receptor region, concurrent field measurements were conducted at a suburban site of Hong Kong and a remote maritime site over the SCS in autumn 2013 (Figure 1). The suburban Tung Chung (TC, 22.29° N, 113.94° E) site, located

in southwestern Hong Kong, was selected as the continental source site, where highly emitted O_3 precursors and O_3 episodes were often observed, particularly in autumn (Cheng *et al.*, 2010; Jiang *et al.*, 2010; Ling *et al.*, 2013; Xue *et al.*, 2014; Wang *et al.,* 2017b). The distance from TC to the Hong Kong International Airport, urban center of Hong Kong and Macau is about 3 km, 20 km and 38 km, respectively. Moreover, TC site belongs to the Hong Kong Environmental Protection Department (HKEPD) air quality monitoring network, in which high quality online data are measured. The measurement instruments were installed in a room on the rooftop of a building (~27.5 m above ground level). Additional details for TC site have been described elsewhere (Cheng *et al.*, 2010; Jiang *et al.*, 2010; Wang *et al.*, 2017b).

In contrast, the maritime Wanshan Island (WSI, 21.93° N, 113.73° E) site, which is bounded to the north by the Pearl River Estuary, was chosen as the receptor site. The island is right in the downwind direction of the PRD region in autumn and winter, when the northeast monsoon prevails (Ling *et al.*, 2013; Wang *et al.*, 2017b). During this period, WSI is regarded as a receptor site of TC, which provides a unique opportunity to evaluate O_3 formation during the transport of air masses from the continental region to the maritime atmosphere. The straight distance is about 44 km between WSI and TC. The island has an area of 8.1 km^2 and a population of about 3,000 with sparse anthropogenic emissions. The sampling instruments were installed at the top floor of the National Marine Environmental Monitoring Station. The height was about 65 m above sea level and ~10 m above ground level.

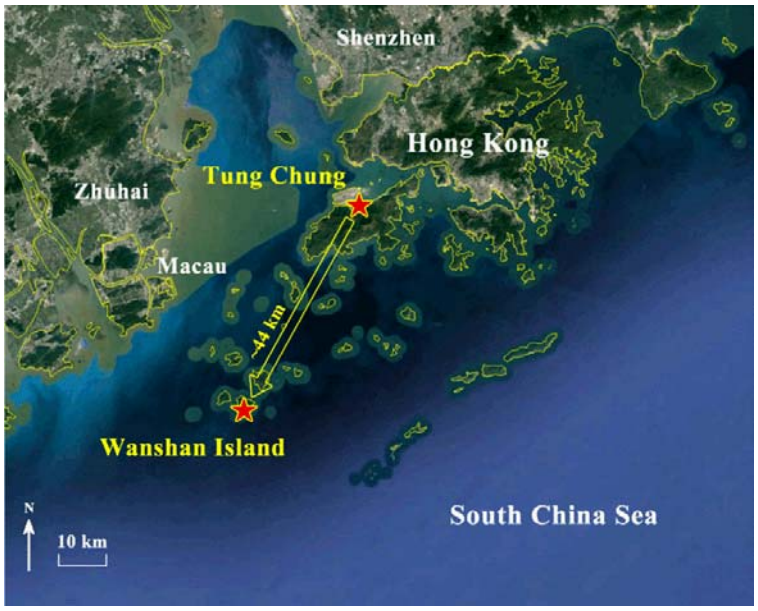

Figure 1. Location of the sampling sites (Tung Chung and Wanshan Island).

2.2 Measurement techniques

2.2.1 Measurements of trace gases and meteorological parameters

At the WSI site, trace gases (*i.e.* O_3, NO-NO_2, CO and SO_2) were continuously monitored with commercial analyzers developed by Advanced Pollution Instrumentation (API) Inc. Briefly, O_3, NO-NO_2, CO and SO_2 were monitored with UV photometric O_3 analyzer, chemiluminescence NO/NO_2/NO_x analyzer, gas filter correlation trace level CO analyzer and UV fluorescence SO_2 analyzer, respectively. The time solution of all instruments was 1 minute. The instrument mode and detection limit are listed in Table 1. More information of quality assurance and control protocols for these devices can be found in our previous studies (Guo *et al.*, 2009; Guo *et al.*, 2013; Wang *et al.*, 2018a). In addition, meteorological parameters (*i.e.* temperature, relative humidity, solar radiation, wind speed and wind direction) were routinely monitored by a weather station (Vantage Pro 2 plus, Davis Instruments) with a time resolution of 5 minutes. At the TC site, hourly data of the aforementioned trace gases and meteorological parameters were obtained from the HKEPD

(http://epic.epd.gov.hk/ca/uid/airdata). The descriptions of the quality assurance and control protocols are provided in the HKEPD report (HKEPD, 2015).

Table 1 Descriptions of O_3, NO-NO_2, CO and SO_2 analyzers

trace gas	Equipment	Model	Detection limit
O_3	UV absorption O_3 analyzer	*API, Model 400E*	0.6 ppbv
NO-NO_2	Chemiluminescence NO/NO_2/NO_x analyzer	*API, Model 200E*	0.4 ppbv
CO	Gas filter correlation trace level CO analyzer	*API, Model 300E*	0.02 ppmv
SO_2	UV fluorescence SO_2 analyzer	*API, Model 100E*	0.4 ppbv

2.2.2 Sampling and analysis of VOCs

During the sampling period, non-methane hydrocarbons (NMHCs) and carbonyls were collected simultaneously at both sites for 21 days, including both non-O_3 episode and O_3 episode days. An O_3 episode day is defined as the day with the peak one-hour averaged O_3 mixing ratio exceeding 100 ppbv (Grade II, China National Ambient Air Quality Standard). 1-hr NMHCs canister samples and 2-hr carbonyl cartridge samples were simultaneously collected every two hours during 7:00 – 19:00 at each site. Intensive NMHCs sampling was also carried out at WSI on selected seven days (*i.e.*, 3, 4, 9 and 22-25 October) with eleven one-hour samples per day (every two hours during 1:00 – 22:00 inclusive). In total, 311 valid VOC samples (144 at TC and 167 at WSI) and 227 carbonyl samples (124 at TC and 103 at WSI) were collected. More descriptions of the VOC sampling can be found in Wang *et al.* (2018a).

The whole-air samples of NMHCs were collected using 2-L electro-polished stainless steel canisters. The canisters were cleaned, conditioned and evacuated before being used for

sampling. A metal bellows pump was used to fill up the canisters with sample air over one-hour integration (with a flow restrictor) to a pressure of 40 psi. The speciation and abundance of 59 C_2-C_{11} NMHCs in the canisters were determined by a Model 7100 preconcentrator (Entech Instruments Inc., California, USA) coupled with an Agilent 5973N gas chromatography-mass selective detector/flame ionization detector (GC-MSD/FID, Agilent Technologies, USA). The detection limit of NMHCs was 3 pptv with a measurement precision of 2-5%, and a measurement accuracy of 5%. Detailed information of the analysis system, and quality control and quality assurance for VOC samples can be found elsewhere (Simpson *et al.*, 2010).

Carbonyl samples were collected using silica gel filled cartridges impregnated with acidified 2,4-dinitrophenylhydrazine (DNPH). An O_3 scrubber was connected to the inlet of the DNPH–silica gel cartridge to prevent interference from O_3. Air samples were drawn through the O_3 scrubber and cartridge for two hours. Before and after each sampling, the flow rate through the cartridges was measured with a rotameter to keep the range of 0.4–0.6 L min^{-1}. All cartridges were stored in a refrigerator at 4 °C after sampling. The sampled carbonyl cartridges were eluted slowly with <5 ml of acetonitrile in the direction opposite to sampling flow into a 5-ml brown volumetric flask, followed by adding acetonitrile to a constant volume of 5 ml. A 20-µl aliquot was injected into the high performance liquid chromatography (HPLC) system through an auto-sampler. Typically, C_1–C_9 carbonyl compounds were measured efficiently with a detection limit of ~0.2 ppbv.

2.3 Photochemical trajectory model (PTM)

2.3.1 General description

In this study, the photochemical O_3 formation processes during the transport of air masses from TC to WSI site were simulated by running a photochemical trajectory model (PTM)

incorporating the MCM. Briefly, the PTM calculates chemical reactions within a well-mixed boundary layer air parcel. The air parcel moves through the pre-defined trajectory and sequentially picks up emissions from each located grid cell of anthropogenic and biogenic VOCs, CO, NO_x and SO_2, and experiences photochemical and depositional processes. In addition, the observed values of meteorological parameters (temperature and relative humidity) were used to constrain the model (Guo *et al.*, 2013; Ling *et al.*, 2014; Lyu *et al.*, 2015a, b). For each trajectory simulation, the model was run for a 13-hr period between 0700 and 1900LT (local time, LT) to calculate the daytime photochemical O_3 formation according to the MCM mechanism.

2.3.2 Master chemical mechanism

The MCM is a near-explicit chemical mechanism, involving 5,900 chemical species and around 16,500 reactions. Previous studies demonstrate that the MCM performs well in calculating the O_3 production (Jenkin *et. al.*, 1997, 2003; Saunders *et. al.*, 2003). Facsimile software (Curtis and Sweetenham, 1987) is used to integrate the model system of differential equations with integration output set each hour. The model output simulates mixing ratios of O_3, O_3 precursors, radicals (*i.e.* OH, HO_2, RO and RO_2), and intermediates. The initials of O_3 and its major precursors were set up as follows according to the observations during the sampling period and previous studies: O_3 (40 ppbv), NO (10 ppbv), NO_2 (20 ppbv), CO (600 ppbv), methane (1.79 ppmv), ethane (1.5 ppbv), propane (2.0 ppbv), ethene (2.0 ppbv), propene (0.6 ppbv), ethyne (4.5 ppbv), toluene (3.0 ppbv), *m,p*-xylene (1.5 ppbv), formaldehyde (5.0 ppbv), and acetaldehyde (2.0 ppbv) (Guo *et al.*, 2004, 2007; Barletta *et al.*, 2005; Wang *et al.*, 2008; Cheng *et al*., 2010).

2.3.3 Emission inventory

The model simulation was based on the combination of the 2006-based PRD emission inventory (3×3 km) (Zheng *et al.*, 2009) and an emission inventory for Hong Kong compiled by Hong Kong Environmental Protection Department (HKEPD). The inventories included six sources, namely gasoline vehicle exhaust, diesel vehicle exhaust, solvent usage, gasoline evaporation and LPG usage, biomass and coal burning, and biogenic emissions, and all the sources had speciated VOC profiles containing 92 VOCs (Liu *et al.*, 2008; Zheng *et al.*, 2009). According to Zheng *et al.* (2009), the speciated VOC source profiles in the emission inventories were mainly established on the basis of measurements of 158 samples collected from the emission sources by Liu *et al.* (2008). The temporal and diurnal variations of emission profiles for on-road mobile sources can be found in Zheng *et al.* (2009), while for biogenic source they were given by Zheng *et al.* (2010) and Situ *et al.* (2010), respectively. Since only 59 VOC species were measured in this study, the summed emission of each of the 59 VOC species from the six sources was individually input into the PTM-MCM for model simulations.

2.3.4 Settings of physical modules

Apart from the module of chemical reactions, photolysis rate, dry deposition and the boundary layer height are all considered in the PTM. The photolysis rates of different chemicals in the model are parameterized using the photon flux determined from the Tropospheric Ultraviolet and Visible Radiation (TUVv5) model (Lam *et al.*, 2013), while the dry deposition module includes the dry deposition of air pollutants, which are parameterized as an average deposition rate within the mixed layer height (MLH). The MLH is assumed to vary from 300 m at night to 1400 m during the daytime (Lam *et al.*, 2013). More detailed descriptions of the model are provided in Cheng *et al*. (2010), Guo *et al*. (2013) and Ling *et al*. (2014). The transport process within the PTM is illustrated using backward trajectory

analysis. Respective backward trajectories arriving at WSI were calculated using NOAA-HYSPLIT4.8 (Draxler and Rolph, 2012) for 1-hr intervals to the end point of 200 m above sea level (Guo *et al.*, 2009; Cheng *et al.*, 2010). The horizontal dimensions of the air parcel were 3 × 3 km, which is consistent with the resolution of emission inventory.

2.3.5 Model performance

Similar to previous modeling studies (Wang *et al.*, 2015; Lyu *et al.*, 2015a, b, 2016; Wang *et al.*, 2017b), the index of agreement (IOA) was applied to evaluate the model performance. The IOA is defined as follows (Equation 1) (Huang *et al.,* 2005; Wang *et al.*, 2015; Lyu *et al.*, 2015a, b).

$$\mathrm{IOA} = 1 - \frac{\sum_{i=1}^{n}(O_i - S_i)^2}{\sum_{i=1}^{n}(|O_i - \bar{O}| + |S_i - \bar{O}|)^2} \quad \text{(Eq. 1)}$$

where S_i and O_i represent simulated and observed values, respectively; ō represents the mean of observed values, and *n* is the number of samples. The IOA value lies between 0 and 1. The better agreement between simulated results and observed data is, the higher the IOA value is (Huang *et al.*, 2005).

3 Results and discussion

3.1 General features of O_3 episodes over the SCS

An overview of this sampling campaign (August–November 2013) was given by Wang *et al.* (2018a). This study mainly focused on the O_3 episodes at both TC and WSI, when continental high pressure dominated and north winds transported polluted continental air masses to maritime atmosphere (Wang *et al.*, 2018a, b). Figure 2(a) displays daily average backward trajectories of air masses on 8 O_3 episode days (red lines) and 13 non-episodes (blue lines) at WSI during the sampling campaign when VOCs samples were measured. Clearly, on all O_3 episode days at WSI, the air masses originated from the inland. Moreover, the hourly

backward trajectory in Figure 2 (b) shows that the air masses passed through the TC site and then arrived at WSI, resulting in the concurrent O_3 episodes at both sites. Since 17 of 21 O_3 episode days (at WSI) intensively occurred in October during the sampling period, mainly due to the impact of two continental anticyclones (Wang *et al.*, 2018a), the days when trace gases and VOCs were both monitored in this month were selected for further investigation. Table 2 shows the daytime (0700-1900 LT) average levels of pollutants during the O_3 episodes (2-4, 22-25 October) and non-episodes (9-10, 17, 30-31 October) at TC and WSI. The TVOCs was defined as the sum of 73 measured VOC species (Table S1). Compared to non-O_3 episodes, higher levels of O_3 and its precursors (*i.e.* NO_2, CO, SO_2 and TVOC) were found during O_3 episodes. The maximum O_3 was around 110 ppbv and 130 ppbv at TC and WSI, respectively, indicating severe O_3 pollution in October. Moreover, the elevated anthropogenic precursors at WSI during episode events also implied that the invaded continental precursors profoundly changed the atmospheric composition and influenced the secondary O_3 formation over the coastal marine areas (Wang *et al.*, 2018a). As such, the PTM-MCM was applied to simulate O_3 formation during the transport of air masses from TC to WSI in the next section.

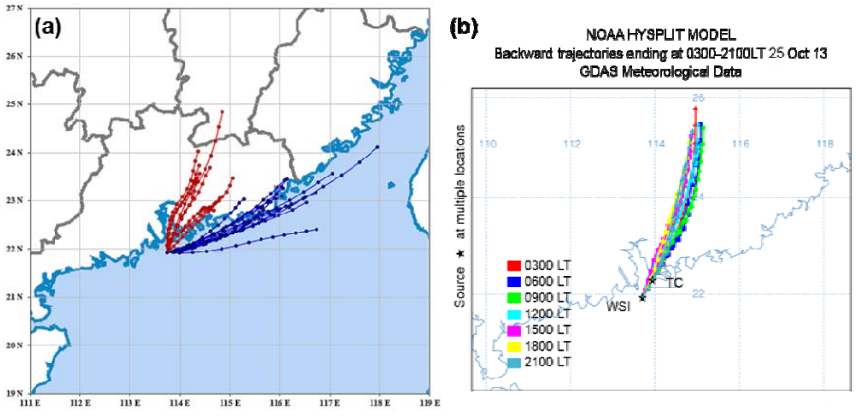

Figure 2. (a) Daily average backward trajectories of air masses on 8 O_3 episode days (red lines) and 13 non-episodes (blue lines) at WSI during the VOC sampling days; (b) Hourly

backward trajectories of air masses arriving at WSI on 25 October 2013. The backward hour of each trajectory in (a) and (b) are 12 hr and 24 hr, respectively. The hourly trajectories of other VOC sampling days in October are given in Figure S1.

Table 2. Descriptive statistics of air pollutants on O_3 episode and non-O_3 episode days in October 2013 at TC and WSI sites (Average ± 95% C.I.; unit: ppbv; C.I.: Confidence Interval). Max. O_3 refers to the average of daily maximum O_3. The average values were calculated during daytime hours (0700-1900LT).

	TC		WSI	
	O_3 episode	Non-O_3 episode	O_3 episode	Non-O_3 episode
Max. O_3	112.8±9.7	61.8±6.8	128.6±15.7	75.7±5.5
O_3	62.5±4.3	44.1±2.9	88.1±4.3	63.4±2.4
CO	691±14.2	500±20	408±12.3	210±10
NO	9.5±1.4	7.6±1.2	0.6±0.1	0.5±0.2
NO_2	37.1±1.7	24.2±1.5	7.1±0.6	1.3±0.4
SO_2	9.7±0.4	6.6±0.2	4.7±0.2	2.2±0.1
TVOCs	19.4±1.7	11.7±1.9	17.6±1.4	8.1±2

3.2 Model construction and comparision with observations

Prior to the study of O_3 formation and its photochemistry over the SCS, the PTM-MCM model performance was evaluated. Figure 3 compares day-to-day patterns of simulated and observed O_3 on the 12 days at TC and WSI. In general, the model well presented the diurnal variations of O_3 at TC and WSI with the same trends as the observations, and the discrepancy between the simulated and observed values was in the range of ±30%. The simulated values were generally lower than the observations. The IOA of the 12-day simulation at TC and WSI was 0.75 and 0.83, respectively, suggesting that the PTM-MCM model, which considered boundary layer trajectories, precursor emissions and chemical processes, provided a

283 reasonable simulation of O_3 formation in the coastal area. Moreover, the simulated precursors
284 were compared with the observations at TC and WSI on the seven O_3 episode days in
285 October 2013. Figure 4 displays the diurnal variations of simulated and observed NO, NO_x
286 and TVOC at TC and WSI. The simulated NO, NO_x and TVOC values presented the same
287 magnitudes as the corresponding observations, and the diurnal variations were consistent. In
288 addition, the simulated VOC species (*i.e.* ethene, ethane, 1-butene, benzene, toluene,
289 formaldehyde and acetaldehyde) had good agreement with the observed values, which are
290 shown in Figure S2.

291 The above differences between the observations and simulation results were likely caused by
292 the following reasons: (1) High vertical gradients of NO_x whereas the PTM assumes that
293 pollutants are completely mixed in the vertical direction; (2) The uncertainties in the 2006-
294 based PRD emission inventory, which showed medium to high uncertainty for the NO_x
295 emission and high uncertainty for VOC and CO emissions (Zheng *et al.*, 2009); (3) The same
296 profiles and fractions of VOC emission sources used for both sites, which in fact were
297 different; (4) The uncertainties of speciated VOC source profiles and the initial settings of
298 precursors used in the model, which influenced the O_3 formation; (5) The emission cell
299 extracted by backward trajectory which might vary; and (6) The physical processes, such as
300 horizontal and vertical dispersion, which were not considered in the PTM-MCM.

301 In summary, the above results indicated that the PTM-MCM was acceptable for the
302 simulations of O_3 and its precursors during the movement of air from TC to WSI. Hence, the
303 process analysis of O_3 photochemistry and the influences of its precursors were further
304 investigated.

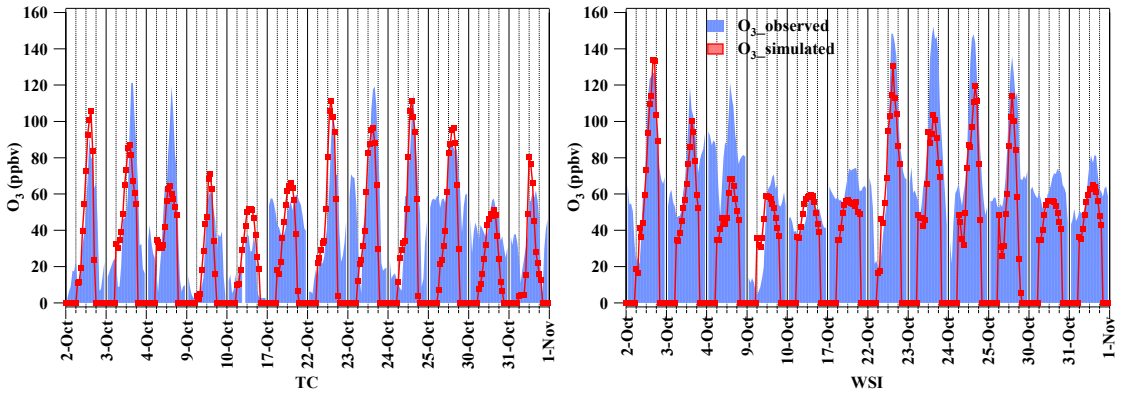

Figure 3. Comparison of observed O_3 (blue shaded areas) with simulated O_3 (red lines) at TC and WSI.

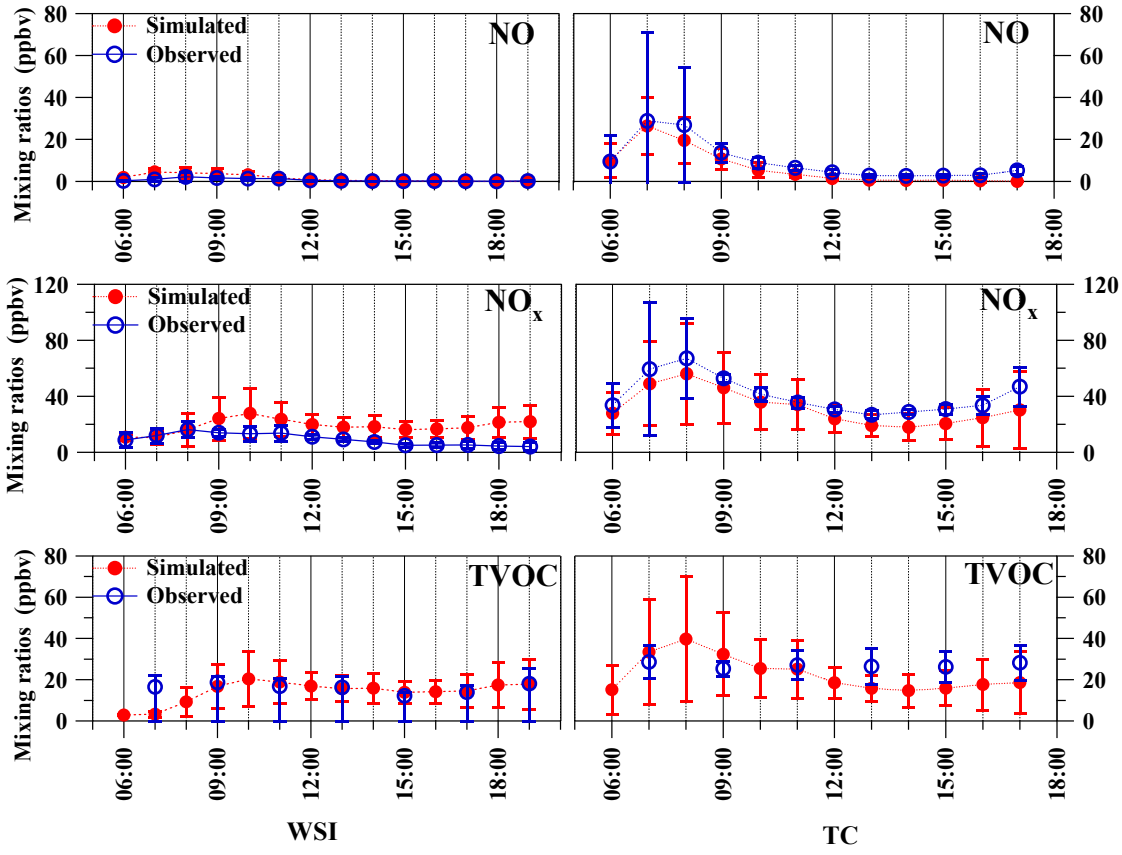

Figure 4. Comparison of observed precursors (blue lines and markers) with simulated precursors (red lines and markers) at TC and WSI.

3.3 Process analysis of O_3 formation from TC to WSI

3.3.1. Temporarily evolutionary variations of O_3 and its precursors

According to the hourly backward trajactories of air masses on each VOC sampling day (Figure S1), 5 days (*i.e.* 2, 22-25 October) when air parcels passed through TC and arrived at WSI were selected for process analysis. Given the 44 km distance between TC and WSI and the daytime average wind speed of 3.9±0.2 m/s on the selected five O_3 episode days, it would take approximately three hours for air parcel at TC to reach WSI. This was consistent with the backward trajectory results, which found that the air parcel from TC to WSI took about three hours (Figure S1).

Figure 5 displays temporarily evolutionary variations of simulated and observed O_3 and its precursors from TC to WSI. Obviously, after the 3-hr transport of air masses from TC to WSI, the simulated precursors (*i.e.* NO, NO_2 and TVOC) decreased intensively in the morning (1000-1200LT), while simulated O_3 increased steadily and the increment sustained high till 1500LT. The maximum decrements of the three simulated precursors occurred simultaneously in the morning, caused by the large variations of mixing ratios at the two sites due to the 3-hr time lag. At TC, the early morning peaks of simulated precursors (0700-0900LT) were consistent with their observations, such as NO (Figure 4), ethene, ethane and other VOCs shown in Figure S2, mainly due to the morning rush-hour emissions and the variation of boundary layers in the morning (So and Wang, 2003; Guo *et al.*, 2013). During the transport processes from TC to WSI, these precursors emitted in early morning at TC experienced the most intensive sunlight and were consumed by the most efficient photochemical reactions during daytime period (Figure 6a, b), resulting in the largest decrements before arriving at WSI at 1000-1200LT. The maximum $\Delta_{precursors}$ values (differences of NO/NO_2/TVOCs between WSI and TC, with a 3-hr time lag) on these 5 days appeared at 1200LT, 1100LT, 1100LT, 1000LT and 1000LT, respectively. Accordingly, O_3

presented the maximum increments at 1100-1400LT, indicating daytime strongest photochemical O_3 formation. The calculated largest Δ_{O3} value (differences of O_3 between WSI and TC, with a 3-hr time lag) was 45.7 ppbv on 22 October, followed by 45.0, 37.5, 36.2 and 34.7 ppbv on 2, 24, 25 and 23 October, respectively. The Δ_{O3} began to decrease in early afternoon and turned to be negative around 1600-1800LT. The averaged negative Δ_{O3} value (-19.7±8.9 ppbv) was much less than the averaged positive Δ_{O3} (39.8±5.6 ppbv) before 1600LT (p<0.05), implying the net O_3 production in these five days. Indeed, the daytime averaged Δ_{O3} (0900-1800LT) was 22.7±8.1 ppbv, which was comparable to the difference of observed O_3 between TC and WSI (26.5±3.1 ppbv, p>0.05), suggesting the contribution of continental precursors to O_3 formation (more than 20 ppbv on average in these 5 days) over the SCS.

To further reveal the changes of O_3 and its precursors from TC to WSI, the temporarily evolutionary variations of radicals and photochemical pathways during the 3-hr transport were illustrated in the next section.

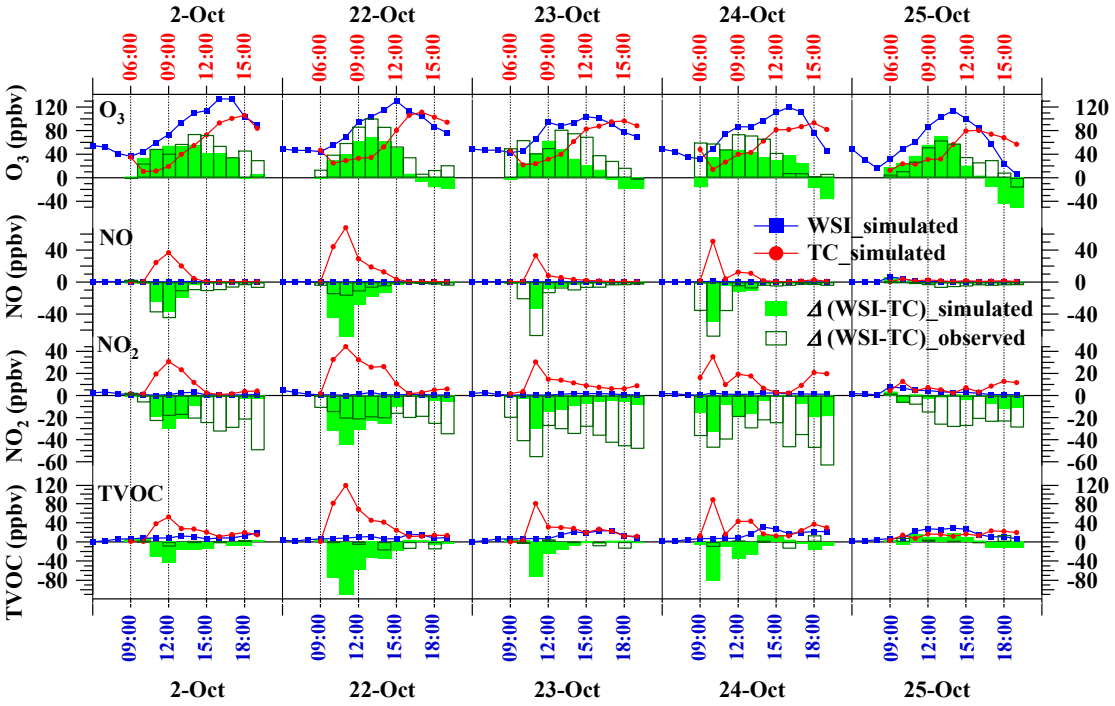

Figure 5. Temporarily evolutionary variations of simulated O_3 and its precursors (*i.e.* NO,

353 NO_2 and TVOC) from TC (red lines and markers) to WSI (blue lines and markers) on 2, 22-
354 25 October 2013. The solid green bars represent the differences between mixing ratios of
355 simulated air pollutants at TC and those after 3 hours at WSI, while the unfilled green bars
356 are the observed differences. Note that the simulated values at TC and WSI correspond to the
357 top (red) and bottom (blue) axis, respectively, and the time lag is 3 hours.

358

359 **3.3.2. Temporarily evolutionary variations of radicals and photochemical pathways**

360 Figure 6(a) presents the temporarily evolutionary variations of simulated OH and HO_2
361 radicals from TC to WSI on the five episode days. Unlike the process analysis of O_3 and its
362 precursors from TC to WSI, radicals cannot be transported due to their short lifetime (<1
363 minute). During the process from TC to WSI, both Δ_{OH} and Δ_{HO2} (differences of radicals
364 between WSI and TC, with a 3-hr time lag) were positive before 1500LT on these five days,
365 with an average increment of $7.6\pm1.7 \times 10^6$ molecules cm^{-3} and $3.7\pm9.1 \times 10^7$ molecules cm^{-3},
366 respectively, whereas Δ_{OH} and Δ_{HO2} became negative after 1500LT, with values of $-4.8\pm1.3 \times$
367 10^6 molecules cm^{-3} and $-5.9\pm4.4 \times 10^7$ molecules cm^{-3}, respectively. Clearly, both Δ_{OH} and
368 Δ_{HO2} were overall positive, indicating that the radicals over the SCS were higher than those
369 on the continent. In addition, the time when maximum OH radicals and maximum
370 photochemical reaction rates appeared was consistent with the maximum decrements of the
371 three precursors (Figure 5).

372 Figure 6(b) illustrates the evolutionary variations of photochemical pathways during the 3-hr
373 transport from TC to WSI. The pathways of VOC+OH initialized the photochemical
374 reactions. Subsequently, HO_2 and RO_2 radicals were generated. The reactions of HO_2+NO
375 and RO_2+NO competed with O_3+NO, resulting in the preservation of O_3. Overall, the
376 temporarily evolutionary variations of photochemical pathways from TC to WSI were similar

to those of radicals; Namely, photochemical O_3 production was accelerated in the morning and at noon, with positive values of averaged Δ_{VOC+OH}, Δ_{HO2+NO} and Δ_{RO2+NO} (6.0±1.5, 5.9±1.5 and 7.8±2.0 × 10^7 molecules cm^{-3}, respectively), but decelerated after 1500LT with negative values of -2.7±0.8, -3.0±0.7 and -4.2±1.0 × 10^7 molecules cm^{-3}, respectively. Since the acceleration rates were much higher than the decelerate rates (p<0.05), the overall photochemical O_3 production during the daytime hours increased from TC to WSI, causing higher O_3 levels at WSI.

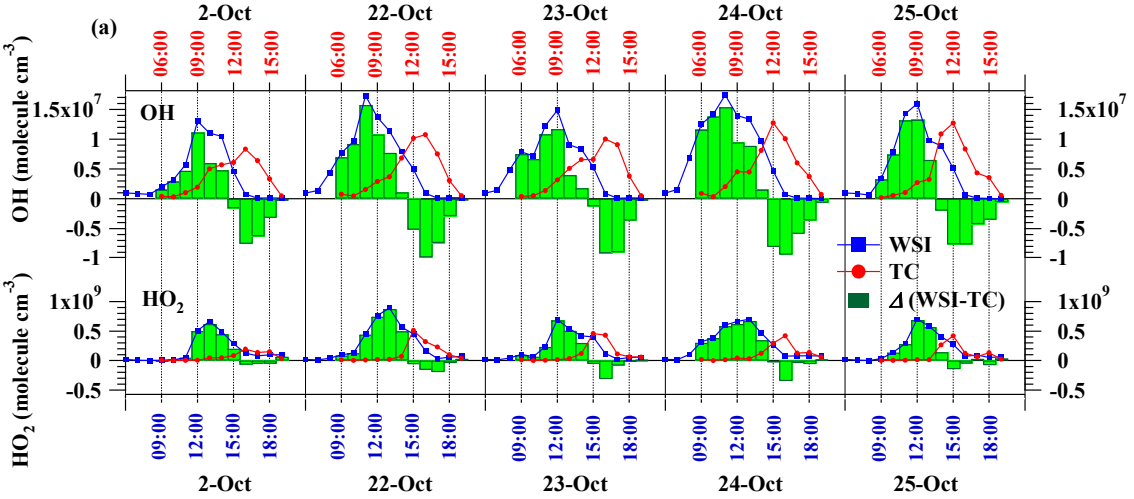

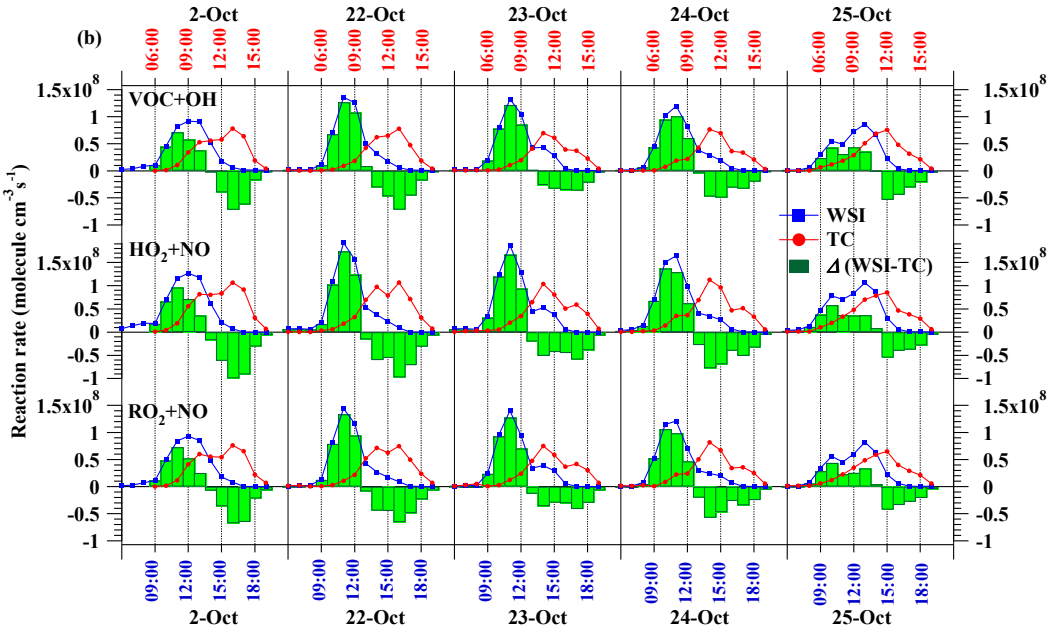

Figure 6. Temporarily evolutionary variations of simulated (a) OH and HO_2 radicals, and (b) major photochemical pathways (*i.e.* VOC+OH, HO_2+NO and RO_2+NO) from TC (red lines and markers) to WSI (blue lines and markers) on 2, 22-25 October 2013. Note that the simulated values at TC and WSI correspond to the top (red) and bottom (blue) hours. The green bars represent the differences between levels of radicals and photochemical formation pathways at TC and those after 3 hours at WSI.

3.3.3. Spatial evolutions of radicals and O_3 photochemistry

Figure 7 shows the spatial evolutions of the average diurnal variations of the simulated OH and HO_2 from TC to WSI. To display the evolutionary processes between the two sites, the diurnal patterns of radicals at 15 km and 30 km (from the TC site) are presented as well. The highest concentration of OH was $9.7\pm2.5\times10^6$ molecules cm^{-3} at TC. After the air mass left the TC site towards the WSI site, the highest OH concentration changed to $1.2\pm0.3\times10^7$ at the location of 15 km and $1.3\pm0.2\times10^7$ at the location of 30 km to TC. Eventually the highest OH level reached $1.4\pm0.1\times10^7$ molecules cm^{-3} at WSI, about 1.5 times that at TC ($p<0.05$). Similarly, the highest HO_2 increased from $3.5\pm1.3\times10^8$ molecules cm^{-3} at TC to $6.8\pm1.1\times10^8$ molecules cm^{-3} at WSI ($p<0.05$). The increase of OH and HO_2 levels from TC to WSI was mainly due to the consumption (*i.e.* the reaction of HO_2+NO) and dilution of NO_x mixing ratios from the continental site to the SCS, which regulated the temporal variations of radicals at different locations. The increased gradients of radicals from TC to WSI reflected that the atmospheric oxidative capacity over the SCS was greater than that on the continent, leading to more intensive O_3 production in the maritime environment.

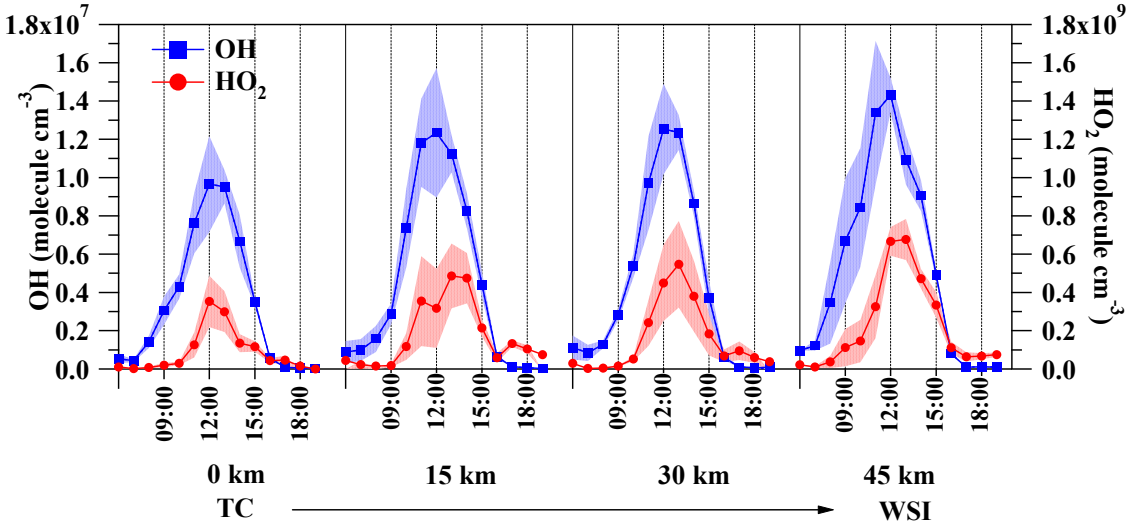

407

408 Figure 7. Spatial evolutions of the average diurnal variations of the simulated OH and HO_2
409 radicals from TC to WSI. The shaded area indicates the 95% Confidence Interval of the
410 averages.

411 Figure 8 depicts the spatial evolutions of the simulated diurnal profiles of O_3 production and
412 destruction rates from TC to WSI. Overall, with the distance farther away from the TC site,
413 the reaction rates of O_3 production/destruction were gradually faster. Consequently, the
414 averaged maximum net O_3 production rate at WSI was $2.0\pm0.5\times10^8$ molecules cm^{-3}, much
415 larger than that at TC ($1.3\pm0.2\times10^8$ molecules cm^{-3}, $p<0.05$). The increase of net O_3
416 production rate from TC to WSI was mainly due to the enhancement of RO_2/HO_2 radicals,
417 which accelerated the photochemical cyclings and resulted in more O_3 production.
418 Sepcifically, O_3 production was dominated by the reaction of HO_2 with NO, with an average
419 contribution of 58.1% and 57.5% at TC and WSI, respectively, while the NO oxidation by
420 RO_2 accounted for 41.9% and 42.5%, respectively. In contrast, the reactions of OH+NO_2 and
421 O_3 photolysis were the major contributors to O_3 destruction at TC with an average
422 contribution of 69.9% and 18.2%, respectively, while their contributions at WSI were 66.1%
423 and 20.1%, respectively. The contribution changes of the O_3 destruction pathways were

mainly attributed to higher NO_2 level at TC, which facilitated the production of HNO_3 via the terminal reaction of OH and NO_2.

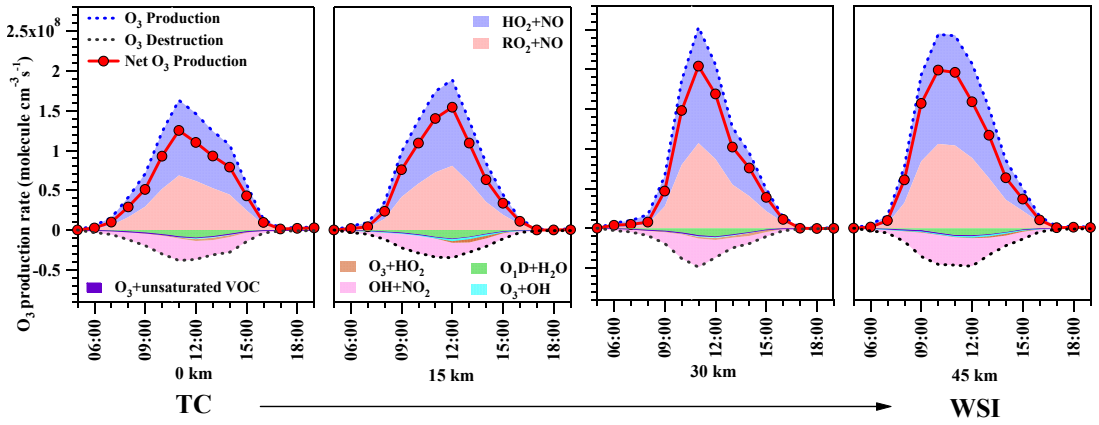

Figure 8. Spatial evolutions of simulated O_3 production and destruction rates from TC to WSI.

3.4 Contributions of continental VOC sources to maritime O_3 formation

Figure 9 shows the speciated profiles of six major VOC sources used in the 2006 emission inventory (Liu *et al.* 2008). As described in section 2.3.3, the six sources were gasoline vehicle exhaust, diesel vehicle exhaust, solvent usage, gasoline evaporation and LPG usage, biomass and coal burning, and biogenic emissions, which contributed 38.4%, 3.2%, 26.8%, 3.3%, 2.5% and 25.8% to total VOC emissions, respectively (Liu *et al.*, 2008; Zheng *et al.*, 2009).

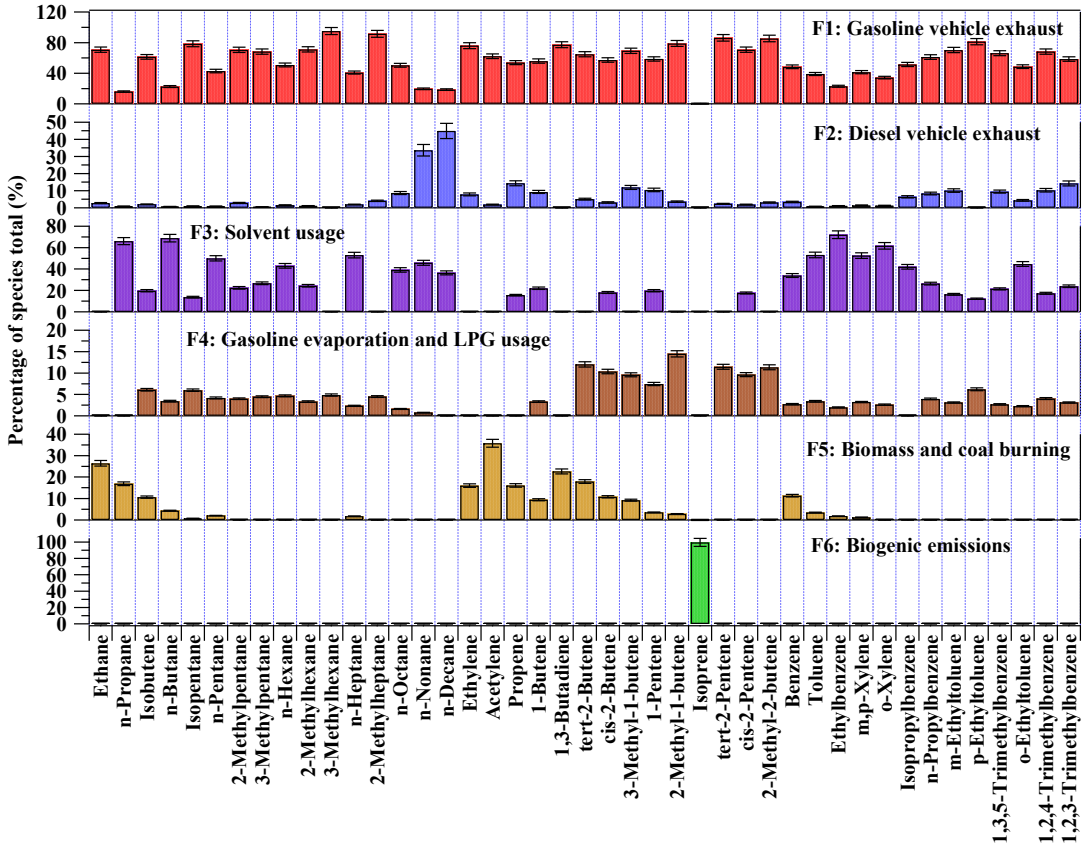

Figure 9. Speciated profiles of the six major VOC sources in the emission inventory, shown in the percentage of species total. Error bars indicate the 95% Confidence Interval of the averaged percentages.

Since O_3 formation was VOC-limited over the SCS on episode days (Wang *et al.*, 2018b), to evaluate the contribution of VOC sources to O_3 formation, two scenarios were designed for data analysis. The first scenario was "base case", which used original emission inventory as input. The second scenario was "constraint case", which excluded each of the six sources in turns from the emission inventory in the "base case". The excluded proportions of each VOC source in the six sources were based on the source profiles in Figure 9. Hence, the contribution of each VOC source was obtained from the difference of simulated O_3 between the "base case" and the corresponding "constraint case". Figure 10 shows the contributions of the six continental VOC sources to photochemical O_3 production at TC and WSI. It was

found that the gasoline vehicle exhaust, solvent usage, and biogenic emissions made large contributions to O_3 formation at TC and WSI, which contributed 8.7±1.7, 6.4±1.2 and 6.1±0.8 ppbv at TC, and 13.9±2.7, 10.2±2.0 and 6.2±0.9 ppbv at WSI, respectively. The contributions of diesel vehicular exhaust, biomass and coal burning, and gasoline evaporation and LPG usage were insignificant at TC and WSI (<2 ppbv).

Since the simulated maritime O_3 formation during the process from TC to WSI was the accumulatively formed O_3 along the upwind locations including TC and the in-situ formed O_3 from the residuals of continental precursors arriving at WSI, the difference of O_3 between WSI and TC was the net contribution of each continental VOC source to maritime O_3 formation. The estimated contributions of gasoline vehicle exhaust and solvent usage emitted at TC to O_3 at WSI were about 5.2 ppbv and 3.8 ppbv, respectively, which dominated the contributions of continental sources to maritime O_3 formation. The large contributions of the aforementioned two sources were mostly attributed to the high reactivity and large abundance of aromatics (above 70%, shown in Figure 9). Moreover, the contributions of alkenes in vehicle exhausts to O_3 formation were not insignificant due to their high reactivity (Atkinson and Arey, 2003). Previous studies already revealed the significant contributions of VOC emissions from gasoline vehicle exhaust and solvent-related sources to O_3 formation in the PRD region (Liu *et al.*, 2008; Guo *et al.*, 2011; Ou *et al.*, 2015; Lyu *et al.*, 2017; Wang *et al.*, 2017b). This study for the first time demonstrated the significant influence of these two sources on the maritime O_3 formation over the SCS. In contrast, because isoprene, the major component of biogenic emissions, has the highest reactivity among VOCs with short lifetime (<2 hours), it was consumed rapidly to form O_3. As such, the continentally-emitted isoprene at TC and upwind locations would be run out before arriving at the maritime WSI site, leading to negligible contribution of continental biogenic emissions to maritime O_3 formation. It is noteworthy that the PTM-MCM model simulation might overestimate the contribution of

VOC sources to O_3 formation due to the use of the same profiles and fractions of VOC emission sources (extracted from the 2006 emission inventory) at the two sites with very different land-use functions (Figure S3).

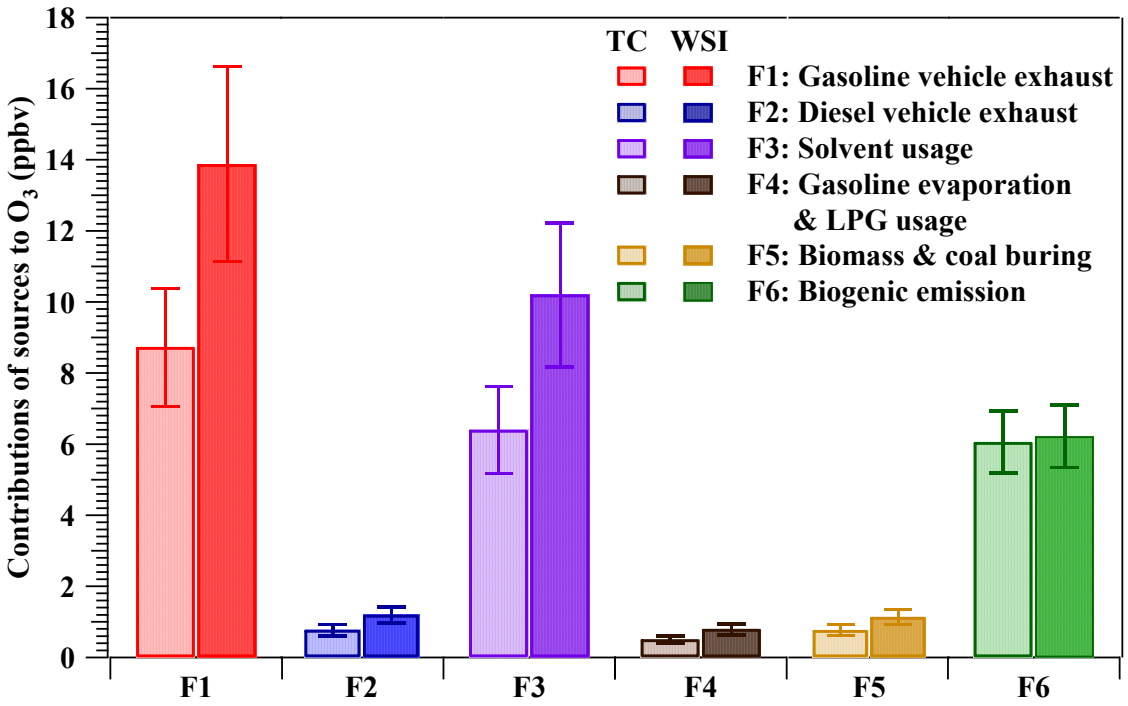

Figure 10. Contributions of six VOC sources to O_3 formation at TC (light-colored bar) and WSI (dark-colored bar). Error bars are the 95% Confidence Intervals of the overall averaged contrbutions.

4 Conclusions

In this study, a PTM model coupled with a near-explicit chemical mechanism was applied to simulate the O_3 formation during the process of transport from a continental site to a maritime site, and to assess the impact of continental VOC sources on O_3 formation over the SCS. According to the backward trajectory analysis, five O_3 episode days at WSI (*i.e.* 2, 22-25 October, 2013), when air masses passed by both TC site of Hong Kong and marine receptor WSI site, were selected to simulate the photochemical processes with the application of PTM. The simulated O_3 and its precursors (*i.e.* NO, NO_2 and VOCs) showed a reasonable

agreement with the observed ones at TC and WSI, indicating that simulated O_3 formation processes from TC to WSI were acceptable. The process analysis of simulated O_3 formation from TC to WSI showed that (1) the precursors decreased significantly in the morning through photochemical consumption and atmospheric dilution; (2) radicals (*i.e.* OH and HO_2) increased and photochemical reactions were accelerated from TC to WSI; and (3) net O_3 production increased from TC to WSI and the daytime average O_3 increment was about 22.7 ppbv from TC to WSI. In addition, based on the source profiles of the emission inventory, the contributions of six sources, namely gasoline vehicle exhaust, diesel vehicle exhaust, gasoline evaporation and LPG usage, solvent usage, biomass and coal burning, and biogenic emissions, to maritime O_3 formation were evaluated. The results for the first time proved that gasoline vehicle exhaust and solvent usage, which contained relatively high reactive aromatic VOC species, largely contributed to O_3 formation over the SCS (~5.2 and 3.8 ppbv, respectively). This study provides insightful method to assess the photochemical evolution of air masses from the continent to the maritime environment, and the impact of continental VOC sources on maritime O_3 formation over the SCS. The findings are helpful to formulate and implement appropriate O_3 reduction strategies.

Acknowledgements

This work was supported by the National Key R&D Program of China (2017YFC0212001), the Research Grants Council (RGC) of the Hong Kong Government of Special Administrative Region (PolyU5154/13E, PolyU152052/14E, PolyU152052/16E and CRF/C5004-15E), and the Hong Kong Polytechnic University PhD scholarships (project #RTTA). This study is partly supported by the Hong Kong PolyU internal grant (1-BBW4 and G-YBUQ).

References

Atkinson, R., and Arey, J., 2010. Atmospheric degradation of volatile organic compounds, Chem. Rev., 103, 4605-4638.

Barletta, B., Meinardi, S., Rowland, F.S., Chan, C.Y., Wang, X.M., Zou, S.C., Chan, L.Y., Blake, D.R., 2005. Volatile organic compounds in 43 Chinese cities. Atmos. Environ. 39, 5979-5990.

Cheng, H.R., Guo, H., Wang, X.M., Saunders, S.M., Lam, S.H., Jiang, F., Wang, T.J., Ding, A.J., Lee, S.C., Ho, K.F., 2010. On the relationship between ozone and its precursors in the Pearl River Delta: application of an observation-based model (OBM). Environ. Sci. Pollut. Res. 17, 547-560.

Curtis, A.R., Sweetenham, W.P., 1987. FACSIMILE release H user's manual. AERE Report R11771 (HMSO), London.

Draxler, R. R., Rolph, G. D., 2003. HYSPLIT (HYbrid Single-Particle Lagrangian Integrated Trajectory) Model access via NOAA ARL READY. NOAA Air Resources Laboratory, Sliver Spring, Maryland, USA. http://www.arl.noaa.gov/ready/hysplit4.html

Finlayson-Pitts, B.J., Pitts, J.N., 1993. Atmospheric chemistry of tropospheric ozone formation: scientific and regulatory implications. Air Waste 43, 1091-1100.

Guo, H., Ling, Z.H., Cheng, H.R., Simpson, I.J., Lyu, X.P., Wang, X.M., Shao, M., Lu, H.X., Ayoko, G., Zhang, Y.L., Saunders, S.M., Lam, S.H.M., Wang, J.L., Blake, D.R., 2017. Tropospheric volatile organic compounds in China. Sci. Total Environ. 574, 1021-1043.

Guo, H., Jiang, F., Cheng, H.R., Simpson, I.J., Wang, X.M., Ding, A.J., Wang, T.J., Saunders, S.M., Wang, T., Lam, S.H.M., Blake, D.R., Zhang, Y.L., Xie, M., 2009. Concurrent observations of air pollutants at two sites in the Pearl River Delta and the implication of regional transport. Atmos. Chem. Phys. 9, 7343-7360.

Guo, H., Wang, T., Louies, P. K. K., 2004. Source apportionment of ambient non-methane hydrocarbons in Hong Kong: Application of a principal component analysis/absolute principal component scores (PCA/APCS) receptor model. Environ. Pollut. 129(3), 489-498.

Guo, H., Ling, Z.H., Cheung, K., Jiang, F., Wang, D.W., Simpson, I.J., Barletta, B., Meinardi, S., Wang, T.J., Wang, X.M., Saunders, S.M., Blake, D.R., 2013. Characterization of photochemical pollution at different elevations in mountainous areas in Hong Kong. Atmos. Chem. Phys. 13, 3881-3898.

Guo, H., So, K.L., Simpson, I.J., Barletta, B., Meinardi, S., Blake, D.R., 2007. C_1 to C_8 volatile organic compounds in the atmosphere of Hong Kong: Overview of atmospheric processing and source apportionment. Atmos. Environ. 41, 1456–1472.

Guo, H., Cheng, H.R., Ling, Z.H., Louie, P. K.K., Ayoko, G.A., 2011. Which emission sources are responsible for the volatile organic compounds in the atmosphere of Pearl River Delta. J. Hazard. Mater. 188, 116–124.

HKEPD (Hong Kong Environmental Protection Department): Air Quality in Hong Kong 2014, 2015. http://www.aqhi.gov.hk/api_history/english/report/files/AQR2014e_Update0616.pdf

Huang, J.P., Fung, J.C.H., Lau, A.K.H., Qin, Y., 2005. Numerical simulation and process analysis of typhoon-related ozone episodes in Hong Kong. J. Geophys. Res. 110, D05301.

Jacob, D.J., 1999. Introduction to Atmospheric Chemistry. Princeton University Press, Princeton, New Jersey.

Jenkin, M.E., Saunders, S.M., Pilling, M.J., 1997. The tropospheric degradation of volatile organic compounds: a protocol for mechanism development. Atmos. Environ. 31, 81-104.

559 Jenkin, M.E., Saunders, S.M., Wagner, V., Pilling, M.J., 2003. Protocol for the development
560 of the Master Chemical Mechanism, MCM v3 (Part B): tropospheric degradation of aromatic
561 volatile organic compounds. Atmos. Chem. Phys. 3, 181-193.
562 Jiang, F., Guo, H., Wang, T.J., Cheng, H.R., Wang, X.M., Simpson, I.J., Ding, A.J., Saunders,
563 S.M., Lam, S.H.M., Blake, D.R., 2010. An ozone episode in the Pearl River Delta: field
564 observation and model simulation. J. Geophys. Res. 115, D22305.
565 Lam, S.H.M., Saunders, S.M., Guo, H., Ling, Z.H., Jiang, F., Wang, X.M., Wang, T.J., 2013.
566 Modelling VOC source impacts on high ozone episode days observed at a mountain summit
567 in Hong Kong under the influence of mountain-valley breezes. Atmos. Environ. 81, 166-176.
568 Li, J.F., Lu, K.D., Lv,W., Li, J., Zhong, L.J., Ou, Y.B., Chen, D.H., Huang, X., and Zhang,
569 Y.H., 2014. Fast increasing of surface ozone concentrations in Pearl River Delta
570 characterized by a regional air quality monitoring network during 2006–2011. J. Environ. Sci.
571 26, 23–36.
572 Ling, Z.H., Guo, H., 2014. Contribution of VOC sources to photochemical ozone formation
573 and its control policy implication in Hong Kong. Environ. Sci. Policy 38, 180-191.
574 Ling, Z.H., Guo, H., Cheng, H.R., Yu, Y.F., 2011. Sources of ambient volatile organic
575 compounds and their contributions to photochemical ozone formation at a site in the Pearl
576 River Delta, southern China. Environ. Pollut. 159(10), 2310-2319.
577 Ling, Z.H., Guo, H., Zheng, J.Y., Louie, P.K.K., Cheng, H.R., Jiang, F., Cheung, K., Wong,
578 L.C., Feng, X.Q., 2013. Establishing a conceptual model for photochemical ozone pollution
579 in subtropical Hong Kong. Atmos. Environ. 76, 208-220.
580 Ling, Z.H., Guo, H., Lam, S.H.M., Saunders, S.M., Wang, T., 2014. Atmospheric
581 photochemical reactivity and ozone production at two sites in Hong Kong: application of a
582 Master Chemical Mechanism-photochemical box model. J. Geophys. Res. 119, 10567-10582.
583 Liu, Y., Shao, M., Lu, S.H., Chang, C.-C., Wang, J.-L., Fu L.L., 2008. Source apportionment
584 of ambient volatile organic compounds in the Pearl River Delta, China: Part II. Atmos.
585 Environ. 42(25), 6261-6274.
586 Lyu, X.P., Chen, N., Guo, H., Zhang, W.H., Wang, N., Wang, Y., Liu, M., 2015a. Ambient
587 volatile organic compounds and their effect on ozone production in Wuhan, Central China.
588 Sci. Total Environ. 541, 200-209.
589 Lyu, X.P., Ling, Z.H., Guo, H., Saunders, S.M., Lam, S.H.M., Wang, N., Wang, Y., Liu, M.,
590 Wang, T., 2015b. Re-examination of C_1-C_5 alkyl nitrates in Hong Kong using an observation-
591 based model. Atmos. Environ. 120, 28-37.
592 Lyu, X.P., Guo, H., Simpson, I.J., Meinardi, S., Louie, P.K.K., Ling, Z.H., Wang, Y., Liu, M.,
593 Luk, C.W.Y., Wang, N., Blake, D.R., 2016. Effectiveness of replacing catalytic converters in
594 LPG-fueled vehicles in Hong Kong. Atmos. Chem. Phys. 16, 6609-6626.
595 Lyu, X.P., Zeng, L.W., Guo, H., Simpson, I.J., Ling, Z.H., Wang, Y., Murray, F., Louie,
596 P.K.K., Saunders, S.M., Lam, S.H.M., Blake, D.R., 2017. Evaluation of the effectiveness of
597 air pollution control measures in Hong Kong. Environ. Pollut. 220, Part A, 87-94.
598 NRC, 1991. Rethinking the Ozone Problem in Urban and Regional Air Pollution. The
599 National Academies Press, Washington, DC.
600 Ou, J.M., Guo, H., Zheng, J.Y., Cheung, K., Louie, P.K.K., Ling, Z.H., Wang, D.W., 2015.
601 Concentrations and sources of non-methane hydrocarbons (NMHCs) from 2005 to 2013 in
602 Hong Kong: a multi-year real-time data analysis. Atmos. Environ. 103, 196-206.
603 Saunders, S.M., Jenkin, M.E., Derwent, R.G., Pilling, M.J., 2003. Protocol for the
604 development of the Master Chemical Mechanism, MCM v3 (Part A): tropospheric
605 degradation of non-aromatic volatile organic compounds. Atmos. Chem. Phys. 3, 161-180.

606 Seinfeld, J.H., Pandis, S.N., 2016. Atmospheric Chemistry and Physics: from Air Pollution to
607 Climate Change, 1232, third ed. Wiley, N. J.
608 Simpson, I.J., Blake, N.J., Barletta, B., Diskin, G.S., Fuelberg, H.E., Gorham, K., Huey, L.G.,
609 Meinardi, S., Rowland, F.S., Vay, S.A., Weinheimer, A.J., Yang, M., Blake, D.R., 2010.
610 Characterization of trace gases measured over Alberta oil sands mining operations: 76
611 speciated C_2-C_{10} volatile organic compounds (VOCs), CO_2, CH_4, CO, NO, NO_2, NO_y, O_3 and
612 SO_2. Atmos. Chem. Phys. 10, 11931-11954.
613 Situ, S.P., Wang, X.M., Alex, G., Chen, F., Chai, Z.W., Wu, Z.Y., Li, Z.Q., 2010. Impacts of
614 errors in meteorological simulations on estimation of isoprene emission. Acta. Sci. Circumst.,
615 30(12), 2383-2391.
616 So, K.L. and Wang, T., 2003. On the local and regional influence on ground-level ozone
617 concentrations in Hong Kong. Environ. Pollut. 123, 307–317.
618 Solberg, S., Simpson, D., Jonson, J.E., Hjellbrekke, A.G., Derwent, R., 2004. EMEP
619 Assessment, Part 1, European Perspective, 6.1 the Oxidant Formation Process and its Long
620 Range Transport. Berlin, October 2004. http://www.bioone.org/doi/abs/10.1579/0044-7447-
621 34.1.2.
622 Wang, T., Lam, K.S., Lee, A.S.Y., Pang, S.W., Tsui, W. S., 1998. Meteorological and
623 chemical characteristics of the photochemical ozone episodes observed at Cape D'Aguilar in
624 Hong Kong. J. Appl. Meteorol. 37 (10), 1167−1178.
625 Wang, T., Wei, X.L., Ding, A.J., Poon, C.N., Lam, K.S., Li, Y.S., Chan, L.Y., Anson, M.,
626 2009. Increasing surface ozone concentrations in the background atmosphere of Southern
627 China, 1994–2007. Atmos. Chem. Phys. 9, 6217–6227.
628 Wang, T., Xue, L.K., Brimblecombe, P., Lam, Y.F., Li, L., Zhang, L., 2017. Ozone pollution
629 in China: A review of concentrations, meteorological influences, chemical precursors, and
630 effects. Sci. Total Environ. 575, 1582-1596.
631 Wang, Y., Wang, H., Guo, H., Lyu, X.P., Cheng, H.R., Ling, Z.H., Louie, P.K.K., Simpson,
632 I.J., Meinardi, S., Blake, D.R., 2017a. Long-term O_3-precursor relationships in Hong Kong:
633 field observation and model simulation. Atmos. Chem. Phys. 17, 10919-10935.
634 Wang, H., Lyu, X.P., Guo, H., Wang, Y., Zou, S.C., Ling, Z.H., Wang, X.M., Jiang, F., Zeren,
635 Y.Z., Pan, W.Z., Huang, X.B., Shen, J., 2018a. Ozone pollution around a coastal region of
636 South China Sea: interaction between marine and continental air, Atmos. Chem. Phys., 18(6),
637 4277-4295.
638 Wang, Y., Guo, H., Zou, S.C., Lyu, X.P., Ling, Z.H. Cheng, H.R., Zeren Y.Z., 2018b.
639 Surface O_3 photochemistry over the South China Sea: Application of a near-explicit chemical
640 mechanism box model. Environ. Pollut. 234, 155-166.
641 Wang, J.L., Wang, C.H., Lai, C.H., Chang, C.C., Liu, Y., Zhang, Y.H., Liu, S., Shao, M.,
642 2008. Characterization of ozone precursors in the Pearl River Delta by time series
643 observation of non-methane hydrocarbons. Atmos. Environ. 42, 6233-6246.
644 Wang, N., Guo, H., Jiang, F., Ling, Z.H., Wang, T., 2015. Simulation of ozone formation at
645 different elevations in mountainous area of Hong Kong using WRF-CMAQ model. Sci. Total
646 Environ. 505, 939-951.
647 Xue, L.K., Wang, T., Louie, P.K., Luk, C.W., Blake, D.R., Xu, Z., 2014. Increasing external
648 effects negate local efforts to control ozone air pollution: a case study of Hong Kong and
649 implications for other Chinese cities. Environ. Sci. Technol. 48, 10769–10775.
650 Zhang, J., Wang, T., Chameides, W.L., Cardelino, C., Kwok, J., Blake, D.R., Ding, A.J., So,
651 K.L., 2007. Ozone production and hydrocarbon reactivity in Hong Kong, Southern China.
652 Atmos. Chem. Phys. 7, 557-573.

Zheng, J.Y., Zhang, L.J., Che, W.W., Zheng, Z.Y., Yin, S.S., 2009. A highly resolved temporal and spatial air pollutant emission inventory for the Pearl River Delta region, China and its uncertainty assessment. Atmos. Environ. 43(32), 5112-5122.

Zheng, J.Y., Zheng, Z.Y., Yu, Y.F., Zhong, L.J., 2010. Temporal, spatial characteristics and uncertainty of biogenic VOC emissions in the Pearl River Delta region, China. Atmos. Environ. 44(16), 1960-1969.